# Tunable visible emission and persistent luminescence of $BaGa_2O_4:Cu^{2+}$

Wang, Lei; Zhao, Ning; Zhu, Changrui; Chen, Lei; Jiang, Yang; Zhou, Rulong; Liu, Yanfang; Qu, Bingyan; Hintzen, Hubertus T.

**DOI**
10.1016/j.cej.2024.149361

**Publication date**
2024

**Document Version**
Final published version

**Published in**
Chemical Engineering Journal

Chemical Engineering Journal 483 (2024) 149361

Contents lists available at ScienceDirect

Chemical Engineering Journal

journal homepage: www.elsevier.com/locate/cej

# Tunable visible emission and persistent luminescence of $BaGa_2O_4:Cu^{2+}$

Lei Wang [a,c,d], Ning Zhao [a], Changrui Zhu [a], Lei Chen [a], Yang Jiang [a], Rulong Zhou [a], Yanfang Liu [e], Bingyan Qu [a,c,*], Hubertus T. Hintzen [b,*]

[a] School of Materials Science and Engineering, Hefei University of Technology, Hefei 230009 Anhui, China
[b] Fundamental Aspects of Materials and Energy, Delft University of Technology, Mekelweg 15, Delft 2629 JB, Netherlands
[c] The Joint Laboratory of the Anhui PingJuDe Medical Technology Co., LTD - Hefei University of Technology, Tongcheng City, Anhui 231400, China
[d] Engineering Research Center of High Performance Copper Alloy Materials and Processing, Ministry of Education, Hefei University of Technology, Hefei 230009, China
[e] Instrumental Analysis Center, Hefei University of Technology, Hefei 230009, China

ARTICLE INFO

*Keywords:*
$Cu^{2+}$ luminescence
Phosphors
Tunable emission
Persistent luminescence
Mechanism

ABSTRACT

In the field of solid-state luminescence, $Cu^{2+}$ has long been widely acknowledged for its capacity to emit infrared light. However, the occurrence of visible emission from $Cu^{2+}$ ions had been infrequently observed and reported. In this study, we made an intriguing discovery by examining the behavior of $Cu^{2+}$ within an irregular coordination environment of Ba in $BaGa_2O_4$. When excited by UV light, $Cu^{2+}$ unexpectedly gave a vibrant yellow–red emission, covering a wavelength range spanning from 500 to 750 nm. More noteworthy, by simply manipulating the excitation wavelength or adjusting the temperature, the peak wavelength of the emission could be effectively tuned from approximately 600 to 660 nm, which could be attributed to the luminescence nature of the charge transfer (CT) between $O^{2-}$ and $Cu^{2+}$. Moreover, the phosphor material displayed a remarkable persistent luminescence (PerL) lasting up to 12 h after UV light excitation. Through thermoluminescence (TL) measurements and first-principle calculations, we found that the intrinsic defects, such as vacancies of oxygen and gallium ($V_O$ and $V''_{Ga}$), played important roles for the PerL phenomena. These findings highlighted the exceptional tunability and PerL properties of $BaGa_2O_4:Cu^{2+}$. Our study provided a new potential guideline for the design of $Cu^{2+}$-activated phosphors in visible region, and opened up new avenues for the research in related functional luminescence materials.

## 1. Introduction

In the field of solid state luminescence, $Cu^{2+}$ ion is often considered as a type of infrared emitter rather than visible one, as it is believed that its emission is from the d-d transition induced by the Jahn-Teller effect. For example, in $KZnF_3$, $Cu^{2+}$ occupies Zn site and is coordinated with six F ions forming $CuF_6$ octahedron. The emission peak is about 1600 nm [1]. In $YGaO_3$, $YInO_3$ and $GdInO_3$, $Cu^{2+}$ is located at Ga or In sites, bonded with five O ions, forming trigonal–bipyramidal structure. The emission spectra of $Cu^{2+}$ exhibit a broad band from 1000 nm to 1600 nm [2]. $Cu^{2+}$ in $CaCuSi_4O_{10}$, at the center of four oxygens square, can emit infrared light peaking at 918 nm [3]. On the contrast, only few reports observed its visible emission so far. For instance, $Cu^{2+}$, occupying the larger $Cs^+$ site in CsBr, exhibits an broad band that features peaks at 486 nm and 582 nm [4], which is ascribed to the electron transition from conduction band to 3d orbital of $Cu^{2+}$. In our previous work, $Cu^{2+}$ at Sr sites in $SrGa_2O_4$ yields a red emission band, peaking at 622 nm [5]. This emission comes from the electron transition from the excited $Cu^{2+}$ to the host valence band. For the case of $SrZrO_3$, $Cu^{2+}$ can induce an orange emission with a peak wavelength of 599 nm and the author assigned this emission to the d-d transition [6]. Considering the energy region of Jahn-Teller effect, the d-d transition could not generate visible light. Although the underlying mechanism of visible emission is largely unclear, from the above observations, it seems that the compact coordinated environment might trigger its infrared emission, while the relative spacious environment can provoke its visible emission. Moreover, $Cu^{2+}$ exhibits a wide span of colors from blue to red depending on the hosts. So, verifying the above assumption through doping $Cu^{2+}$ in a spacious local environment to see how far its emission can be tuned is very insightful not only for the understanding of its emission mechanism but also for the deliberate design of $Cu^{2+}$ activated multi-color materials, as these $Cu^{2+}$ doped phosphors might open up its applications in LEDs,

* Corresponding authors at: School of Materials Science and Engineering, Hefei University of Technology, Hefei, Anhui 230009, P. R. China.
*E-mail addresses:* byqu@hfut.edu.cn (B. Qu), H.T.Hintzen@tudelft.nl (H.T. Hintzen).

https://doi.org/10.1016/j.cej.2024.149361
Received 7 November 2023; Received in revised form 28 January 2024; Accepted 2 February 2024
Available online 5 February 2024

advanced optical sensing and anti-counterfeiting applications in future [7,8].

For this purpose, we take a much larger site, $Ba^{2+}$ for $Cu^{2+}$ to occupy. $BaGa_2O_4$ is an ideal host material, since it can exhibit high-efficiency luminescence when doped with not only lanthanide ions such as: $Sm^{3+}$[9], $Eu^{3+}$[10], $Pr^{3+}$[11], $Dy^{3+}$ [12], but also transition metal ion $Cr^{3+}$[13] and $s^2$ ion $Bi^{3+}$[14]. However, it is still an open question whether the spacious local environment offered by $Ba^{2+}$ ion can ignite the visible emission of $Cu^{2+}$. Moreover, $Cr^{3+}$[13], $Bi^{3+}$[14] and $Sm^{3+}$[9] can exhibit excellent persistent luminescence (PerL) phenomena in this host, implying that the intrinsic defects existing in $BaGa_2O_4$ could serve as efficient trapping centers for PerL. Whether $Cu^{2+}$ ion can cooperate with those intrinsic defects to achieve PerL phenomenon in $BaGa_2O_4$ is also interesting. At present, most of high-efficient PerL materials such as $SrAl_2O_4$:$Eu^{2+}$,$Dy^{3+}$ [15], $CaAl_2O_4$:$Eu^{2+}$,$Nd^{3+}$ [16], $Sr_4Al_{14}O_{25}$:$Eu^{2+}$, $Dy^{3+}$[17], $CaTiO_3$:$Pr^{3+}$ [18], $Ca_2SnO_4$:$Pr^{3+}$ [19], $Lu_2O_3$:$Pr^{3+}$ [20], $Ca_2SnO_4$:$Sm^{3+}$ [21], $(Ca_{1-x}Sr_x)_2Si_5N_8$:$Eu^{2+}$,$Tm^{3+}$ [22], $Sr_3Al_2O_5Cl_2$:$Eu^{2+}$,$Dy^{3+}$ [23] rely on the lanthanides ions in determining the color of the emission and(or) the trap depths. This work might offer a new alternative to the design of rare-earth-free afterglow phosphors.

To substantiate above interesting assumption, we synthesized a series of $BaGa_2O_4$ samples with different Cu ion concentrations by the high-temperature solid state reaction method in this work. Our findings indicate that $Cu^{2+}$ tends to incorporate $Ba^{2+}$ sites with spacious coordination environment and can be excited by UV light at 286 or 347 nm. The emission spectra present a broad band from 500 to 750 nm peaking at approximately 600 nm. Moreover, with the increase of the excitation wavelength from 347 to 390 nm, the emission band exhibits a substantial red-shift from 600 to 660 nm. More strikingly, such a red-shift of emission can also be realized by increasing the temperature from ambient temperature to 200 ℃. In addition, upon a mere 5 min of excitation by both 254 and 365 nm lamps, $BaGa_2O_4$:$Cu^{2+}$ exhibits exceptional brilliant yellow afterglow and the duration of the afterglow can last as long as 12 h, which is comparable with current commercial persistent phosphors. By applying the TL measurements and the First-principle calculations, we find that O vacancy and Ga vacancy can bring about the PerL of $Cu^{2+}$. Contrast to the common knowledge about the infrared emission of $Cu^{2+}$, the observation in this work offers a comprehensive understanding about luminescence property of $Cu^{2+}$ and opens up a whole new mind-set for the exploration of relevant functional materials.

## 2. Method

### 2.1. Materials and synthesis

$Ba_{1-x}Ga_2O_4$:xCu ( $x$ = 0, 0.01, 0.02, 0.03, 0.04, 0.05, 0.06 and 0.07) samples were synthesized with a high-temperature solid state reaction method. All the starting materials, $BaCO_3$ (99.99 %), $Ga_2O_3$ (99.99 %) and CuO (99.99 %), were offered by Aladdin Co., Ltd. Those starting materials were weighed off according to the stoichiometric ratio and ground thoroughly in an agate mortar and then transferred into alumina crucibles. In the muffle furnace, the mixture was heated at 900 ℃ for 3 h and 1350 ℃ for 8 h in static air. The obtained samples were cooled down to the ambient temperature naturally and ground into powder for further characterizations.

### 2.2. Characterization of materials

The X-ray diffraction (XRD) patterns of samples were collected via the PANalytical X'Pert PRO MPD X-ray powder diffraction apparatus, operating at 40 kV and 40 mA, with graphite-monochromatized Cu Kα radiation. The Rietveld refinements of the structure were finished by using the general structure analysis system (GSAS) program. A field emission scanning electron microscope (FE-SEM, JEOL JSM-6 490) was adopted to characterize the powder morphology, EDS and element mapping. The X-ray Photoelectron Spectroscopy (XPS) analyses were fulfilled via an instrument of ESCALAB250Xi (Thermo, USA). The calibration of the peak shift in binding energy was performed against the reference of carbon's 1 s peak at 284.6 eV. The excitation and emission spectra of phosphors were obtained with a fluorescence spectrophotometer (Hitachi FL-4600, Japan) at ambient temperature. The temperature-dependent optical spectra were gathered with an accessory heater manufactured by Orient KOJI instrument Co., Ltd (China). The UV–visible diffuse reflection spectra (DRS) of samples were measured with an ultraviolet–visible-near-infrared (UV–Vis-NIR) spectrophotometer (CARY5000 produced by Agilent). The PerL curves of the samples were measured after 5 min excitation with both 365 and 254 nm lamps (8 W) at ambient temperature utilizing a PR305 instrument from Zheda Sensing Technology Co., Ltd. The TL curves of samples were measured on a FJ-427A1 TL meter (Beijing Nuclear Instrument Factory). Before the TL measurements, the samples were exposed to the ultraviolet radiation with both lamps for five minutes.

### 2.3. Calculation methods

The calculations of formation energies and defect levels of the dopant Cu and the intrinsic defects in $BaGa_2O_4$ were carried out by using the First-principle calculations as implemented in the VASP5.4 code. The Ba($5s^25p^66s^2$), Ga($3d^{10}4s^24p^1$), O($2s^22p^4$) and Cu($3d^{10}4s^1$) were treated as the valence electrons. The GGA-PBE function was adopted to describe the exchange–correlation interactions between the valence electrons. The energy cutoff of the plane wave was 400 eV. The defective structure models were constructed by removing one of the Ba or Ga or O atoms ($V_{Ba}$, $V_{Ga}$, $V_O$) in the unit cell of $BaGa_2O_4$ (with the stoichiometry of $Ba_{24}Ga_{48}O_{96}$), or the replacement of a Ba atom by a Cu atom. A 2 × 2 × 4 Γ-centered k-point mesh was used to sample the Brillouin zone. The formation energies of $Cu^{n+}$ ion (n = 1, 2) in the case of occupying different Ba sites were calculated by using the formula [24]:

$$E_F(Cu^{n+}) = E(BaGa_2O_4 : Cu^{n+}) - E(BaGa_2O_4) - \mu(\mathrm{Cu}) + \mu(Ba) + (\mathrm{n}-2)\varepsilon_f$$

where $E(BaGa_2O_4 : Cu^{n+})$ and $E(BaGa_2O_4)$ were the energies of $BaGa_2O_4$ with and without $Cu^{n+}$, while $\mu_{Ba}$ or $\mu_{Cu}$ was the chemical potentials of Ba or Cu metal, taken as the total energy of one Ba or Cu atom in Ba or Cu metal. Ba or Cu metal crystallizes to BCC structure or FCC structure, respectively. $\varepsilon_f$ was the Fermi level of the system. All the structure models were fully relaxed until the interatomic forces less than 0.01 eV/Å. The optimized lattice constant $a = b$ and $c$ of $BaGa_2O_4$ were 18.615 Å and 8.626 Å, which were in agreement with the experimental values (see below).

## 3. Results and discussion

### 3.1. Phase and crystal structure of $BaGa_2O_4$:Cu

The XRD patterns of $Ba_{1-x}Ga_2O_4$:xCu (x = 0.02, 0.03, 0.04, 0.05, 0.06 and 0.07) were illustrated in Fig. 1(a). They matched well with the standard pattern of $BaGa_2O_4$ (ICSD-91281). The Rietveld refinements of the host and $Ba_{0.95}Ga_2O_4$:0.05Cu were shown in Fig. 1(b, c). The refinement factors $R_{wp}$ and $\chi^2$ converged to 8.44 %, 1.68 and 9.23 %, 1.72, respectively. No impurity phases were observed in obtained samples. $BaGa_2O_4$ crystallized in hexagonal crystalline lattice with space group $P6_3$. The lattice constants were $a = b$ = 18.6477 Å and $c$ = 8.6696 Å. According to the unit cell structure of $BaGa_2O_4$ as shown in Fig. 1(d), the Ba ions occupied six non-identical sites [25]. While, we noted that the doping of Cu slightly shifted the diffraction peaks towards higher degrees as shown in Fig. 1(a). The unit cell volume of $Ba_{1-x}Ga_2O_4$:xCu roughly shrunk with the increase of Cu concentration. The radius of Cu ion (0.60 Å for $Cu^+$ and 0.57 Å for $Cu^{2+}$ in tetrahedral site [26]) is larger than that of $Ga^{3+}$ ion (0.47 Å [26]) located in tetrahedral site, but much

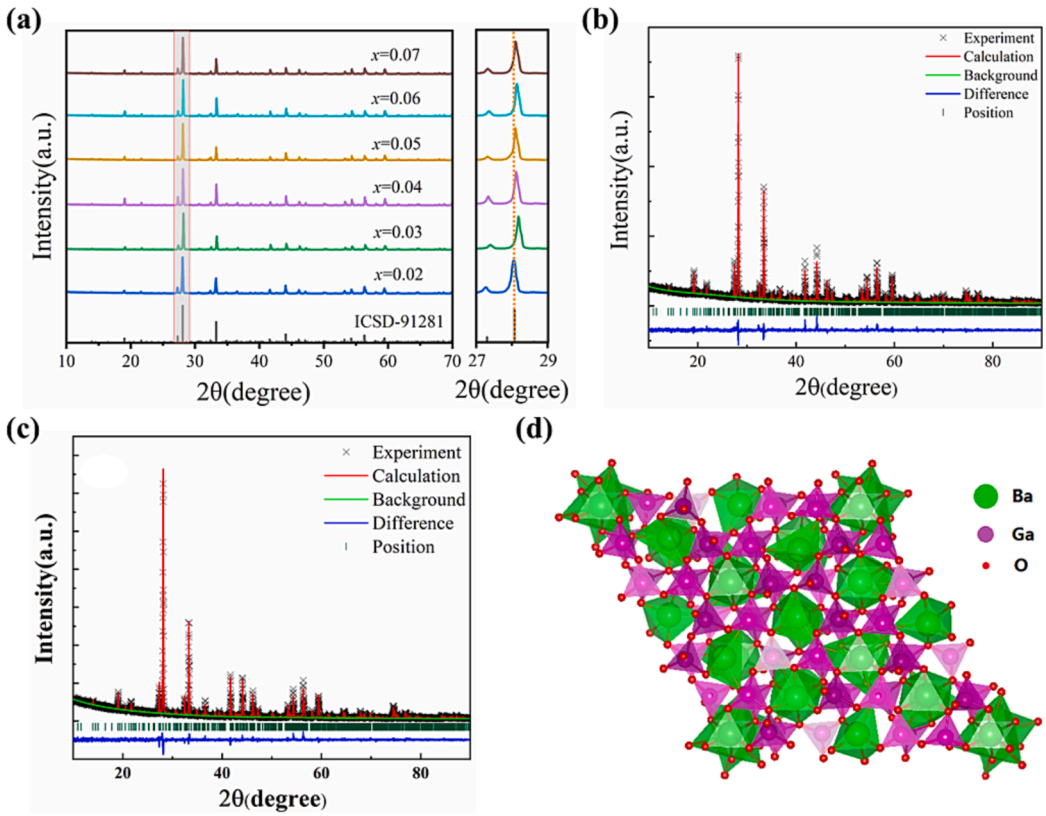


**Fig. 1.** (a) XRD patterns of $Ba_{1-x}Ga_2O_4$:$x$Cu ($x$ = 0.02–0.07). Refined XRD of (b) $BaGa_2O_4$ and (c) $Ba_{0.95}Ga_2O_4$:0.05Cu. (d) Schematic crystal structure of $BaGa_2O_4$.

smaller than that of $Ba^{2+}$ ion (1.42 Å CN = 8 [26]). So, the volume contraction of the unit cell might be due to the occupation tendency of Cu in $Ba^{2+}$ sites.

The SEM morphologies of $BaGa_2O_4$:Cu sample were characterized in Fig. 2(a - c). The particles of the sample displayed irregular shape with size of 10 ~ 20 μm. The elemental mapping images of the sample were shown in Fig. 2(d – g), where Ba, Ga, O and Cu elements distributed in host uniformly.

The charge states of Cu ions doped in solids are often 2 + and(or) 1+, while the luminescence properties for them are different. Therefore, it becomes essential to discern the charge states of Cu ions in $BaGa_2O_4$ prior to characterizing their photoluminescent properties. We tentatively conducted the XPS analysis of $BaGa_2O_4$:Cu to identify their states by the shift of their character bands with Cu concentrations ($x$) as illustrated in Fig. 3. Normally, the 2p3/2 band of $Cu^+$ often locates at a slightly lower energy compared to $Cu^{2+}$. For example, it is about 932.5 eV in $Cu_2O$ [27] and 933.45 eV in CuO [28]. Fig. 3 showed that, at $x$ = 0.03, no significant signal could be discerned due to the low Cu ion concentration. The 2p3/2 band was detected at $x$ = 0.04, with peak energy of about 932.97 eV, between 932.7 eV and 933.1 eV, suggesting the co-presence of both $Cu^+$ and $Cu^{2+}$ in $BaGa_2O_4$. Further, this band shifted towards to higher energy with Cu concentration as indicated by the vertical dotted line, implying an increasing ratio of $Cu^{2+}$ relative to $Cu^+$. Upon reaching $x$ = 0.07, the band energy was approximately 933.34 eV, hereby signifying that Cu ions in $BaGa_2O_4$ mainly exhibited 2 + state. Moreover, the satellite bands at about 943 and 962 eV increased in intensity when $x \geq 0.06$, which were the typical character of $Cu^{2+}$ ion, manifesting the presence of $Cu^{2+}$ in the host.

The calculated formation energies of both $Cu^{2+}$ and $Cu^+$ at different Ba sites were listed in Table 1, where the formation energies of Cu ion at Ba3 site were taken as reference. The formation energies of $Cu^{2+}$ at Ba1, Ba2 and Ba3 were very close and much lower than those at Ba(4 ~ 6), implying $Cu^{2+}$ tended to occupy the former three Ba sites from the consideration of the thermodynamic statistics. This result could be

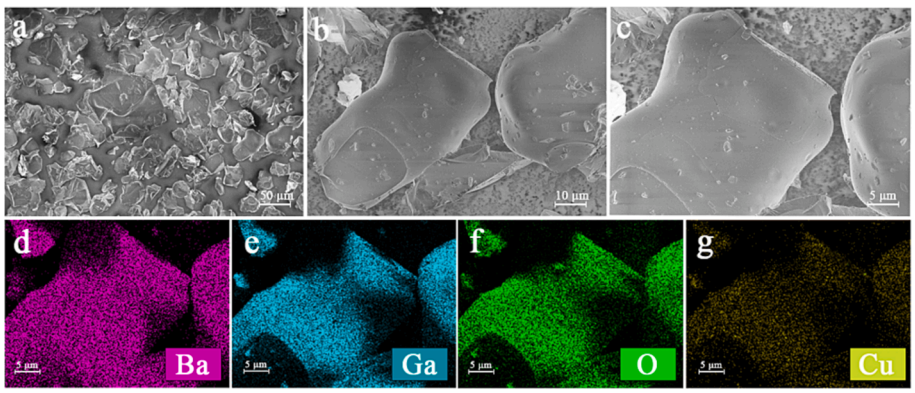


**Fig. 2.** (a - c) SEM morphologies of $Ba_{0.95}Ga_2O_4$:0.05Cu sample. The element mapping images of Ba (d), Ga (e), O (f) and Cu (g) in the sample.

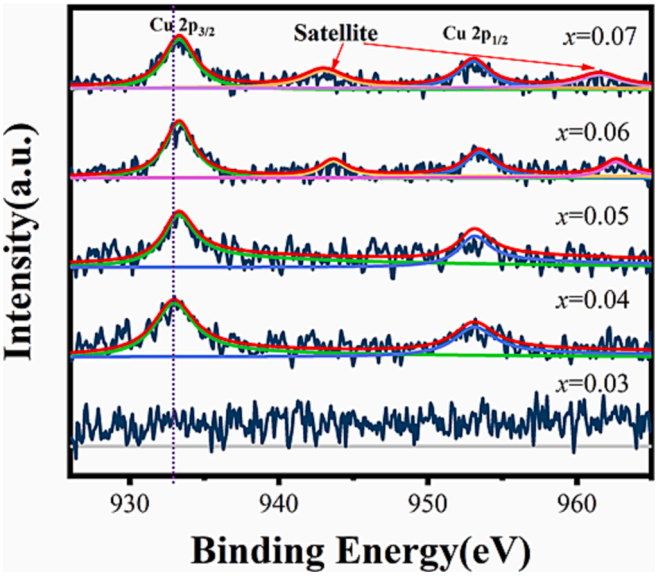


**Fig. 3.** XPS spectra of $Ba_{1-x}Ga_2O_4$:$x$Cu ($x$ = 0.03–0.07).

**Table 1**
Formation energies (eV) of $Cu^{2+}$ and $Cu^{+}$ occupying different Ba sites in $BaGa_2O_4$.

| | Ba1 | Ba2 | Ba3 | Ba4 | Ba5 | Ba6 |
|---|---|---|---|---|---|---|
| $Cu^{2+}$ | 0.088 | 0.126 | 0 | 0.473 | 0.836 | 0.648 |
| $Cu^{+}$ | 0.132 | 0.015 | 0 | 0.400 | 0.531 | 0.282 |

understood since Ba(1 ~ 3) were relatively smaller than those of Ba(4 ~ 6) in volume estimated from the Ba-O bond lengths listed in Table S1 of the Supplementary material (SM). Meanwhile, the ionic radius of Cu ion was much smaller than that of $Ba^{2+}$. Thus, the local structural distortion caused by the replacement of Cu ion at Ba(1 ~ 3) would be relatively less serious. By comparing the formation energies of $Cu^{+}$ listed in Table 1, we reached the same conclusion that $Cu^{+}$ ions most probably distributed at Ba(1 ~ 3). For the local environment, $Cu^{2+}$ was bonded with three $O^{2-}$ ions with the bond lengths of 1.93 ~ 1.98 Å at Ba3 site, forming a near three-coordinated plane, which was shown in Fig.S1 of SM file. Detailed discussion about the local coordination environment was described in SM file.

### 3.2. *Photoluminescent properties of $BaGa_2O_4$:Cu*

Fig. 4(a) presented the DRS of $BaGa_2O_4$ as well as $Ba_{0.95}Ga_2O_4$:$x$Cu ($x$ = 2 ~ 7). The near band absorption at about 250 nm revealed a band gap of about 5.18 eV for undoped $BaGa_2O_4$ evaluated using Kubelka-Munk function [29]. This finding agreed well with 5.04 and 5.16 eV reported in literature [14,30]. A subtle absorption feature, observed at approximately 300 nm in the DRS of $BaGa_2O_4$, potentially came from the intrinsic defects within $BaGa_2O_4$. The DRS of samples with different Cu concentration were nearly identical. A noticeable enhancement in the absorption intensity was seen around 300 nm by Cu doping. Cu also provoked the appearance of some additional absorption bands at about 350, 500 and 700 nm. The bands at 300 and 350 nm could possibly be attributed to the $O^{2-}$ - $Cu^{2+}$ charge transfer (CT) bands, as the CT bands of $Cu^{2+}$ often exhibit two proximate peaks in UV region in several crystalline structures including MgO [31] and LiCl [32], while the bands at about 500 and 700 nm possibly originated from d-d transition of $Cu^{2+}$ considering the d-d absorption often located in green–red and near-infrared regions [3,33].

Upon doping with Cu ion, a higher intensity excitation band peaking around 347 nm and a lower intensity band at around 286 nm with an added shoulder at approximately 250 nm could be observed when monitoring at 602 nm (Fig. 4(b)). The peak at 250 nm could be assigned to the host related excitation and was in good agreement with the excitation spectrum of the host lattice as illustrated in Fig.S2(a) of SM file. In response to the 347 nm excitation, a substantial emission band, ranging from 500 nm to 750 nm, appeared with a peak at 602 nm, which was close to the case of $Cu^{2+}$ in $SrZrO_3$ and $SrGa_2O_4$ at approximately 599 and 622 nm, respectively [5,6]. Thus, we could reasonably conclude that the emission of Cu ion in $BaGa_2O_4$ was dominated by $Cu^{2+}$. We assigned the excitation of $Cu^{2+}$ at 347 nm to the electron transfer from $O^{2-}$ to $Cu^{2+}$, the nature of which was in consistent with the intrinsic excitation of CuO. CuO is a charge-transfer gap semiconductor [34]. Its density of states showed that the highest valence band was mainly from the 2p of O, while the lowest conduction band was dominated by the 3d of Cu [35,36]. In $BaGa_2O_4$: Cu, upon the excitation of 347 nm, an electron transferred from the 2p orbitals of a neighboring $O^{2-}$ to the empty 3d orbital of $Cu^{2+}$, resulting in the creation of a hole ($h$) at the vicinity of $O^{2-}$ ions, as expressed by the following equation,

$$Cu^{2+} + O^{2-} \rightarrow (e.Cu^{2+})^{*} + O^{2-} + h$$

where $(e.Cu^{2+})^{*}$ represented the excited $Cu^{2+}$ with an additional electron occupying the empty 3d orbital. When the hole recombined with $(e.Cu^{2+})^{*}$, yellow light was emitted.

When excited at 286 nm, the shape of the emission spectra was identical to that excited at 347 nm (Fig. 4(b) and (c)). The peak wavelength was about 598 nm. This indicated that both excitation bands at 286 and 347 nm originated from $Cu^{2+}$. As shown in Fig. 4(b, c), the optimal Cu concentration $x$ was 0.05, since both emission bands had the highest intensities at this concentration. Typically, d-d emission of $Cu^{2+}$ is located in infrared region [3,33]. However, given this work primarily concerned the visible emission linked with $Cu^{2+}$, we would not engage in a discussion about the d-d transition of $Cu^{2+}$ here.

As mentioned above, $Cu^{2+}$ ion tended to incorporate predominantly on three Ba sites. Different local environments could result in varying emissions. Consequently, the broad emission spectra would reflect the overlap of $Cu^{2+}$ emissions across these three Ba locations. This assertion found substantiation evidences between the emission spectra and the excitation wavelength, as featured in Fig. 4(d - f). When the excitation wavelength increased from 286 to 347 nm, there was a marginal growth in the emission peak wavelength–only from 598 to 602 nm. Upon reaching an excitation wavelength of 390 nm, a substantial red-shift emerged, extending from 602 up to nearly 660 nm. For further increasing the excitation wavelength, no discernible shift could be observed in the emission wavelength. Conversely, the host-related emission band remained stable at 468 nm regardless of the excitation wavelength fluctuation. To highlight these details, Fig. 4(e) exhibited the normalized main emission bands under excitations from 286 to 390 nm. Monitoring over various wavelengths, from 540 to 660 nm, the normalized excitation spectra were presented in Fig. 4(f). The shapes of these excitation spectra were nearly unchanged with the main excitation peak slightly shifting from 346 to 348 nm. The red-shift of the emission might be due to the different sensitivities of $Cu^{2+}$ ions positioned in different Ba sites to the excitation wavelength.

The emission spectra illustrated in Fig. 4(d) allowed for the estimation of chromaticity coordinates for $Ba_{0.95}Ga_2O_4$:0.05Cu. Upon excitation with 286 nm, the chromaticity coordination was (0.4748, 0.4612), locating within the yellow region of the Commission Internationale de l'Enclairage (CIE) chromaticity diagram depicted in Fig.S3 of SM file. When the sample was subjected to a higher excitation at 347 nm, the coordination shifted to (0.4929, 0.4679). As we continued to increase the excitation wavelength, the color of the sample shifted to the orange region and then towards the blue region. This shift in color could be attributed to an intensity decline of $Cu^{2+}$ emission band coupled with the increase of host-related emission. Fig. 4(d) also integrated photographs of the sample, captured when excited by 254 and 365 nm light

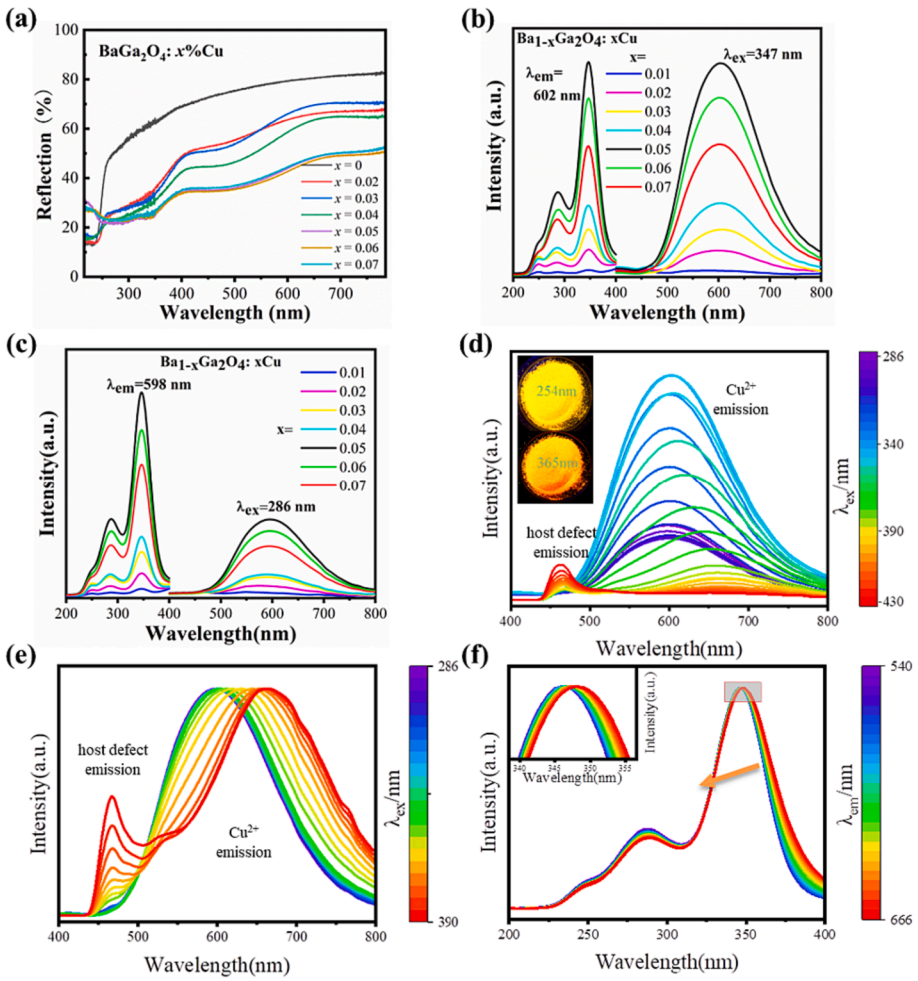


**Fig. 4.** (a) DRS of $BaGa_2O_4$ and $Ba_{0.95}Ga_2O_4$:*x*Cu ($x = 0.02$–$0.07$). The excitation and emission spectra of $Ba_{1-x}Ga_2O_4$:*x*Cu with $\lambda_{em} = 602$ nm, $\lambda_{ex} = 347$ nm (b) and $\lambda_{em} = 598$ nm, $\lambda_{ex} = 286$ nm (c). (d) The emission spectra of $Ba_{0.95}Ga_2O_4$:0.05Cu under the excitation of 286 ~ 430 nm. Insets are the photographs of the sample under the excitation of 254 and 365 nm. (e) The normalized emission spectra of $Ba_{0.95}Ga_2O_4$:0.05Cu under the excitation of 286 ~ 390 nm. (f) The normalized excitation spectra of $Ba_{0.95}Ga_2O_4$:0.05Cu monitored with 540 ~ 660 nm. Inset is the enlarged part of excitation spectra of the 350 nm peak.

sources for comparative illustration. These images provided visual validation for the change in emission spectra corresponding with variations of excitation wavelengths.

The luminescence decay curve of $BaGa_2O_4$:Cu was obtained under excitation of 347 nm. As illustrated in Fig. 5(a), by using the exponential formula: $I = I_0 + I_1\exp\left(-\frac{t}{\tau_1}\right) + I_2 exp\left(-\frac{t}{\tau_2}\right) + I_3\exp(-\frac{t}{\tau_3})$, the lifetime $\tau_1$, $\tau_2$ and $\tau_3$ could be extracted to be 0.0918, 0.2130 and 0.9685 ms, where I was the intensity of emission, $I_0$, $I_1$, $I_2$ and $I_3$ were the constants. The average lifetime $\tau$ was then estimated to be about 0.54 ms by adopting the equation $\tau_{avg} = (I_1\tau_1^2 + I_2\tau_2^2 + I_3\tau_3^2)/(I_1\tau_1 + I_2\tau_2 + I_3\tau_3)$[37].

The temperature-dependent excitation spectra monitored at 602 nm and emission spectra excited at 347 nm were depicted in Fig. 5(b, c) and the temperature-dependent integral emission intensity of $Ba_{0.95}Ga_2O_4$:0.05Cu over the range of 298 to 473 K was depicted in Fig. 5(d). The intensities of both spectra demonstrated a monotonic decrease as the temperature increased, implying the thermal quenching took place. Simultaneously, there was also a notable shift in the emission peak wavelength, moving from 602 nm at 298 K to approximately 660 nm at 473 K. This shift could potentially be attributed to the thermal expansion, since longer $Cu^{2+}$–$O^{2-}$ distance at higher temperature could lower the charge transfer energy and thus red shift was expected. Correspondingly, the excitation peaks at 286 and 347 nm were also red-shifted with increasing temperature.

This result indicated that the emission wavelength of $Cu^{2+}$ in $BaGa_2O_4$ had an incredible temperature- & excitation-dependence, which was exceptional in red region, not only for lanthanide-ion-doped phosphors, but also for most of transition-metal-ion-doped phosphors, including $Cr^{3+}$, $Mn^{4+}$. Such a good tunability may find promising applications in advanced temperature-responsive optical sensing or anti-counterfeiting fields.

### 3.3. *Persistent luminescence properties of $BaGa_2O_4$:Cu*

After irradiating with 254 and 365 nm lamps for 5 min, all samples across varying Cu concentrations exhibited PerL phenomena as depicted in Fig. 6(a). Of these, the sample $Ba_{0.95}Ga_2O_4$:0.05Cu showed the longest afterglow lasting up to 12 h. The afterglow spectrum of $Ba_{0.95}Ga_2O_4$:0.05Cu shown in Fig. 6(b) was almost identical to its emission spectra in Fig. 4(b), implying that the afterglow emission could be attributed to the doped $Cu^{2+}$. Fig. 6(c) displayed photographs of the sample taken at intervals ranging from 1 s to 1 h after removing the lamps. Initially, the sample exhibited bright yellow color, and the intensity of the afterglow gradually waned over time. However, even after one hour, the sample still remained clearly visible. The broad band PerL emission with peak wavelength around 600 nm is rarely observed for most transition metal ions activated phosphors and can be regarded as imperative color supplementary components for present representative commercial afterglow phosphors of $CaAl_2O_4$:$Eu^{2+}$, $Nd^{3+}$ (blue) and $SrAl_2O_4$:$Eu^{2+}$, $Dy^{3+}$ (green) to realize multi-colors afterglow. Moreover,

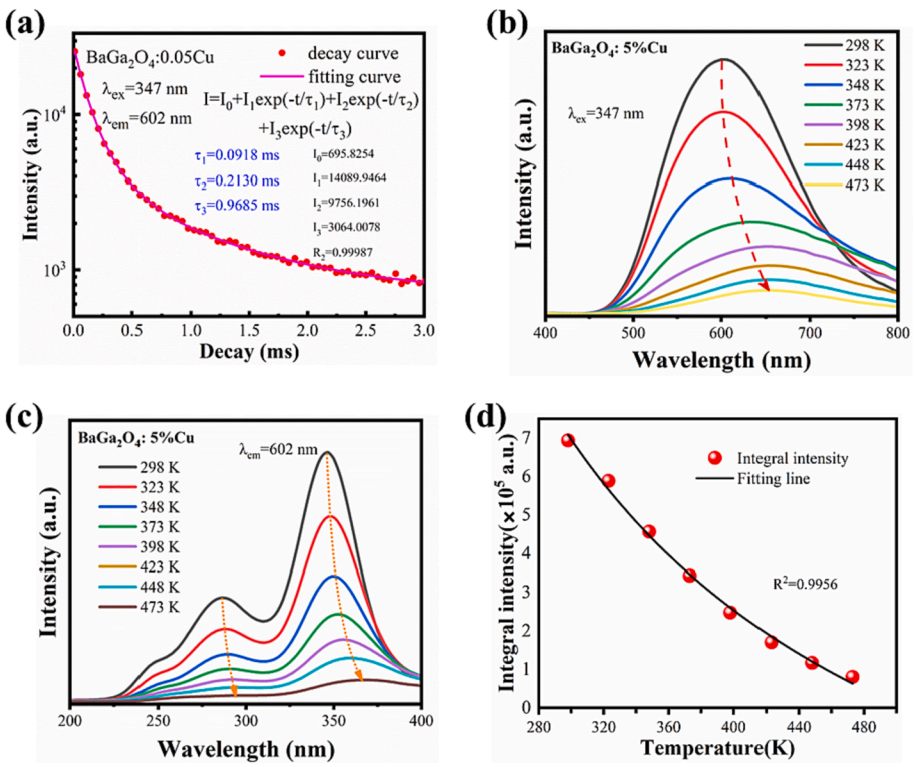


**Fig. 5.** (a) Luminescence decay curve of $Ba_{0.95}Ga_2O_4$:0.05Cu excited at 347 nm. Temperature dependence of emission (b) and excitation (c) spectra for the sample. (d) The integral intensity of the emission excited at 347 nm as a function of temperature.

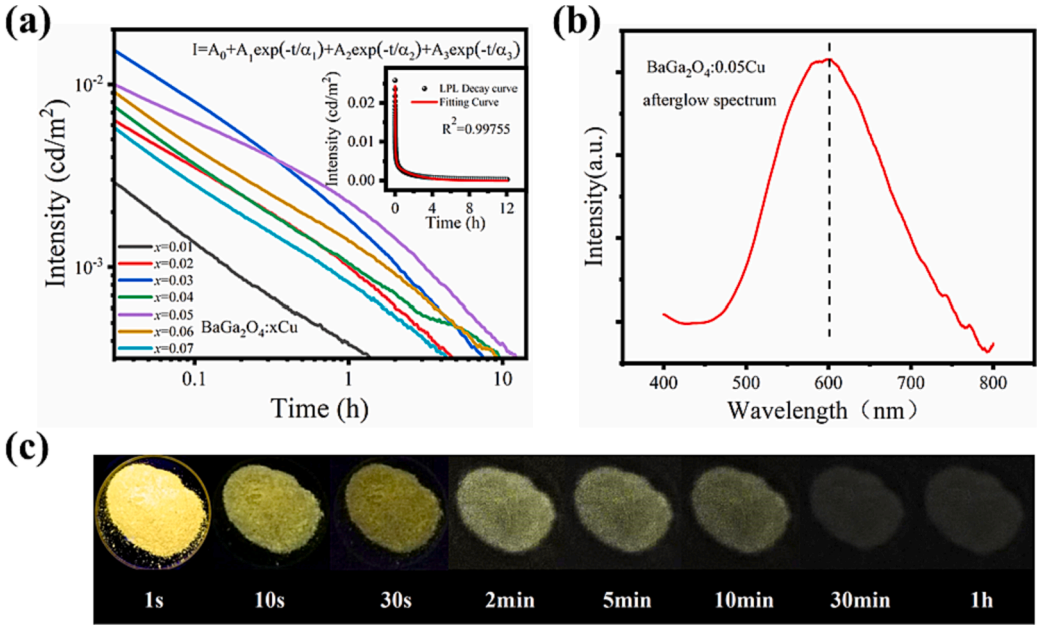


**Fig. 6.** (a) The PerL decay curves of $Ba_{1-x}Ga_2O_4$:$x$Cu ($x$ = 0.01–0.07) after excitation for 5 min by 254 and 365 nm lights. Inset shows the exponentially fitting decay curve for $x$ = 0.05. (b) PerL emission spectrum of $Ba_{0.95}Ga_2O_4$:0.05Cu. (c) PerL photographs of $Ba_{0.95}Ga_2O_4$:0.05Cu taken at different time after removing the excitation sources.

this phorphor is rare-earth-free and cost effective compared with above commercial PerL materials.

The decay curve of $Ba_{0.95}Ga_2O_4$:0.05Cu, taken as an example, could be well fitted by the third-order-exponential function:

$$I = A_0 + A_1\exp\left(\frac{-t}{\alpha_1}\right) + A_2\exp\left(\frac{-t}{\alpha_2}\right) + A_3\exp\left(\frac{-t}{\alpha_3}\right)$$

where I represented the afterglow intensity at time t. $\alpha_1$, $\alpha_2$, and $\alpha_3$ denoted the lifetimes of three different decay processes. $A_1$, $A_2$ and $A_3$ were constants. The fitting result was shown in the inset of Fig. 6(a). We found that $\alpha_1$, $\alpha_2$, and $\alpha_3$ were approximately 30.4 s, 314.5 s, and 7070.1 s, respectively. This suggested the existence of trapping centers with varying depths within the sample.

The TL curves of $Ba_{0.95}Ga_2O_4$:0.05Cu subjected to different heating rates from 1 to 5 K/s were collected after irradiation by both 254 and 365 nm lamps for 5 min. As shown in Fig. 7(a), the recorded data unveiled four different peaks located at approximately 300, 350, 370 and 430 K (termed as P1, P2, P3 and P4, respectively). The depths of the trapping centers (E) corresponding to these four peaks could be estimated using the equation: $\frac{\beta E}{kT_m^2} = sexp(-\frac{E}{kT_m})$ [38,39], where β, k, $T_m$ and *s* were the heating rate, the Boltzmann constant, the peak temperature and the frequency factor. Fig. 7(b) demonstrated the relationships between $\ln(T_m^2/\beta)$ and $1/kT_m$, from which the depths of these four trapping centers were estimated as E = 0.80, 1.22, 1.31 and 1.55 eV, respectively. Obviously, the depths of the first two trapping centers were very suitable for achieving ambient temperature PerL. For the latter two, due to their relatively deeper depths, the confined carriers would be released very slowly at ambient temperature. However, they might play a significant role in the prolonged PerL of the sample.

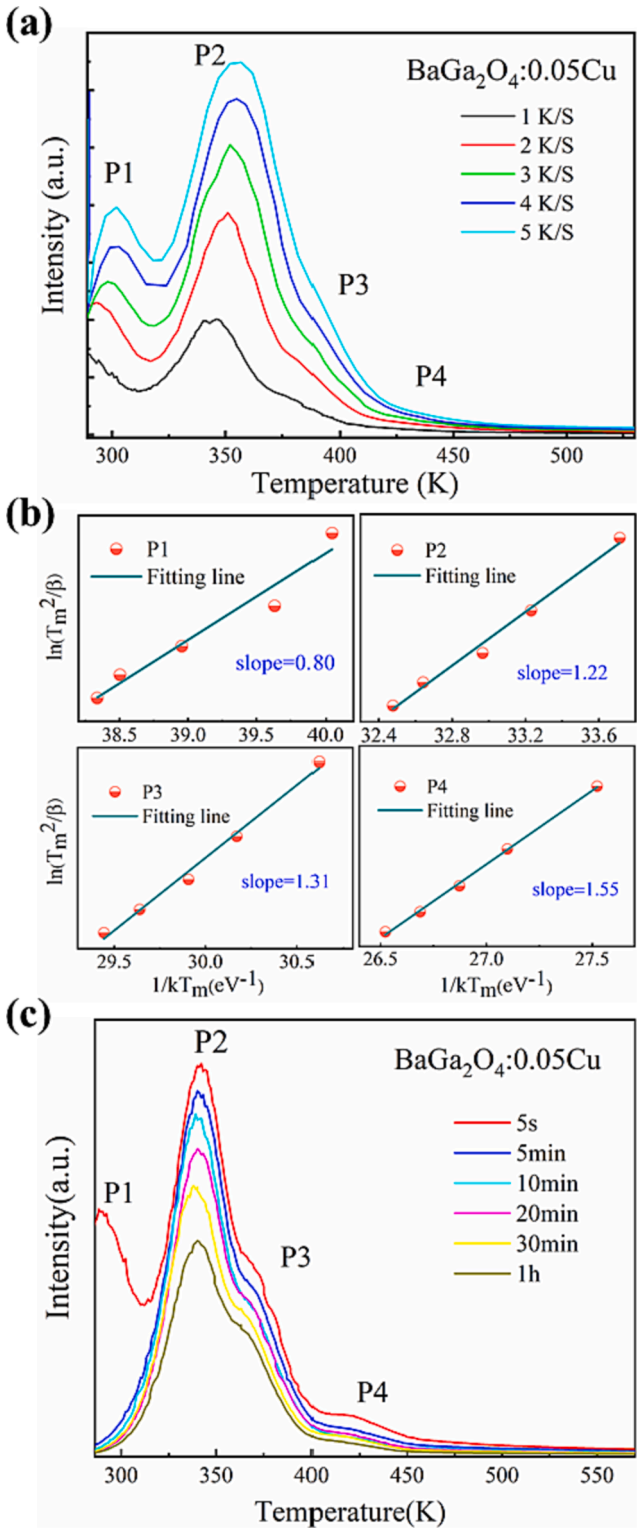


**Fig. 7.** (a) TL spectra of $Ba_{0.95}Ga_2O_4$:0.05Cu collected after irradiation with both 254 and 365 nm for 5 min. (b) Relationships between $\ln(T_m^2/\beta)$ and $1/kT_m$ of the four peaks in (a). (c) TL curves of $Ba_{0.95}Ga_2O_4$:0.05Cu recorded at different decay times after removing the UV lamps.

In order to analyze the carrier-release behavior of the trapping centers, we assessed the TL curves of $Ba_{0.95}Ga_2O_4$:0.05Cu following various decay intervals subsequent to the removal of the UV lamps. As depicted in Fig. 7(c), with the extension of decay time, the TL peak due to trap P1 demonstrated a rapid decrease and almost vanished within 5 min. Conversely, the remaining three traps — P2, P3, and P4 — exhibited a considerably slower rate of decrease. The intensities of the traps P2 and P3 still retained nearly 50 % of the initial intensities at the end of one hour. Upon comparing these results with the PerL decay curves portrayed in Fig. 6(a), it could be inferred that the short-lived decay (with a lifetime of 30.4 s) was likely correlated with the trap P1, while the intermediate PerL phenomena of $Cu^{2+}$ predominantly aligned with traps P2 and P3, as they shared similar trap depths. As to the third decay process with much longer decay lifetime of 7070.1 s, the trap P4 (with a trap depth of 1.55 eV) might have a significant contribution. The considerable depth of this trap could be the plausible explanation for the relatively lower intensity of the long-term afterglow.

A deeper comprehension of PerL mechanism of $Cu^{2+}$ in $BaGa_2O_4$ needed to make clear which defects induced trap levels within the host band. This could be achieved through the utilization of First-principle calculations. Given no foreign impurities had been induced into the host except Cu, we limited our focus on the intrinsic defects of $BaGa_2O_4$, such as: $V_O$, $V_{Ga}$ and $V_{Ba}$, since these vacancies were most likely to emerge in the crystalline oxides when they were synthesized at high temperature [40]. Within $BaGa_2O_4$, there were 16 and 8 non-identical O and Ga atoms. We accounted for each possible non-identical $V_O$, $V_{Ga}$ or $V_{Ba}$ in our calculations. The electronic structure of $V_O$ with the lowest energy was depicted in Fig. 8(a). When compared with a defect-free $BaGa_2O_4$ electronic structure (Fig.S2(b) of SM file), a discernible defect level beneath the Fermi level (our point of reference) arose - this level sat approximately 0.5 eV above the valence band maximum (VBM). Analysis of the partial density of states (PDOS) revealed that this defect level primarily stemmed from the 2p orbitals of $O^{2-}$ ions surrounding the vacancy. The electronic structures of $V_O$ at other O sites were very similar to that in Fig. 8(a). However, they exhibited slightly larger energy differences between the induced defect level and VBM with a range from 0.5 to 1.1 eV. From a thermal dynamic view, electrons located at the defect levels of $V_O$ could transition to the valence band provided holes were present. Consequently, such defect levels might function as hole trapping centers. More interestingly, the energy differences between these defect levels and VBM were ideal for thermal release of the hole back to the valence band.

In a similar manner, $V'_{Ga}$ could generate defect levels in the range of 0.3 ~ 1.0 eV above VBM. A detailed overview of the electronic structures pertaining to Ga vacancies as well as an extensive discussion on the formation energies of both Ga and O vacancies across different charge states could be found in SM file (Fig.S5 and Fig.S6). It was worth noting that Ba vacancies broadly failed to induce any considerable defect levels within the band gap, as evidenced in Fig.S6 in SM file. Besides, the presence of $Cu^+$ in $BaGa_2O_4$ could induce full-occupied defect levels and couldn't act as hole trapping centers as discussed in Fig.S7 in SM file. Summarizing the aforementioned results, we could map out the energy levels diagram for $Cu^{2+}$ and intrinsic defects within $BaGa_2O_4$ as shown in Fig. 8(b). Given the valence band was constructed by the 2p orbitals of

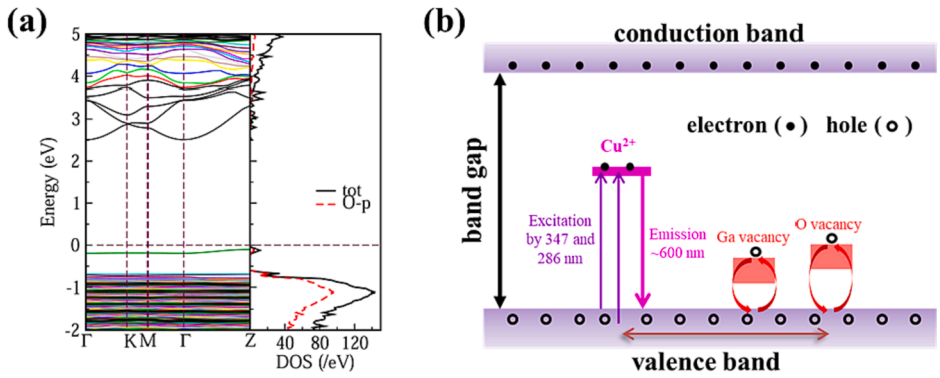


**Fig. 8.** (a) Band structure, total (tot) and partial density of states (2p orbitals of $O^{2-}$, O-p) of $BaGa_2O_4$ with $V_O$. The Fermi level is set to be 0 eV. (b) Schematic illustration of PerL mechanism of $BaGa_2O_4:Cu^{2+}$.

$O^{2-}$ ions and CT process from $O^{2-}$ to $Cu^{2+}$, $Cu^{2+}$ could induce the defect level about 3.57 eV (347 nm) above VBM. $V_O$ and $V''_{Ga}$ formed effective trapping levels. When subjected to excitation, electrons located in valence band transitioned to the defect level associated with $Cu^{2+}$, leaving behind holes in valence band. Subsequently, these holes could directly recombine with electrons situated at the excited state of $Cu^{2+}$, $(e.Cu^{2+})^*$, inciting the emission of yellow light. Alternatively, the holes could get caught by defect levels created by $V_O$ or $V''_{Ga}$. Following thermally-triggered release from these trapping centers, the holes moved back to valence band, and subsequently recombined at $(e.Cu^{2+})^*$ center, leading to a delay in emission and sustaining the PerL of $Cu^{2+}$.

## 4. Conclusions

In summary, we developed a novel type of yellow-emitting PerL phosphor $Ba_{1-x}Ga_2O_4$:xCu by high-temperature solid state reaction method. The excitation spectrum contained two main bands at around 286 and 347 nm ascribed to CT from $O^{2-}$ to $Cu^{2+}$. $Cu^{2+}$ exhibited a very broad band from 500 to 750 nm with the maximum at about 600 nm. The rarely reported yellow PerL arising from $Cu^{2+}$ could last as long as 12 h with the help of the intrinsic defects, like O and Ga vacancies.

The luminescence behaviors of $Cu^{2+}$ in $BaGa_2O_4$ verified that putting $Cu^{2+}$ ion in a spacious coordination environment of $Ba^{2+}$ could effectively provoke its visible emission, especially in the region longer than 600 nm. Remarkably, the emission of $Cu^{2+}$ in $BaGa_2O_4$ exhibited incredible tunability. As the excitation wavelength increased from 347 to 390 nm, the emission shifted from 600 to about 660 nm, covering the whole range of red region. Furthermore, this tunability could also be realized by increasing the temperature from ambient temperature to 200 ℃. Considering these observations and our previous work of $Cu^{2+}$ doped $SrGa_2O_4$, $Cu^{2+}$ demonstrated more tunability since its emission was linked to the energy difference of the host valence band and excited $Cu^{2+}$. Thus, the emission wavelength of $Cu^{2+}$ could be deliberately tuned by modifying the position of the host valence band. This was quite different from the cases of 3d transition metal ions $Cr^{3+}$, $Cr^{4+}$ and $Mn^{4+}$, as their red or infrared emissions were the results of d-d transition in nature and nearly constant with given ligand anions. The observation in this work offered a fresh perspective towards designing $Cu^{2+}$ activated phosphor with visible emission and would spark new avenues of research in related fields.

## CRediT authorship contribution statement

**Lei Wang:** Writing – review & editing, Writing – original draft, Project administration, Investigation, Funding acquisition, Formal analysis, Data curation, Conceptualization. **Ning Zhao:** Writing – original draft, Investigation, Formal analysis, Data curation. **Changrui Zhu:** Investigation, Formal analysis, Data curation. **Lei Chen:** Formal analysis. **Yang Jiang:** Formal analysis. **Rulong Zhou:** Software. **Yanfang Liu:** Formal analysis. **Bingyan Qu:** Writing – review & editing, Writing – original draft, Investigation, Formal analysis, Data curation, Conceptualization. **Hubertus T. Hintzen:** Writing – review & editing, Writing – original draft, Supervision, Formal analysis.

## Declaration of competing interest

The authors declare that they have no known competing financial interests or personal relationships that could have appeared to influence the work reported in this paper.

## Data availability

Data will be made available on request.

## Acknowledgments

This work is supported by the National Natural Science Foundation of China (Grant 52372143), the Industrial Innovation Guidance Fund of Tongcheng City & Hefei University of Technology (JZ2022YDZJ0083) and the Fundamental Research Funds for the Central Universities (PA2022GDGP0029, PA2023GDGP0042). The computation is completed on the HPC Platform of Hefei University of Technology.

## Appendix A. Supplementary data

Supplementary data to this article can be found online at https://doi.org/10.1016/j.cej.2024.149361.

## References

[1] L. Dubicki, M.J. Riley, E.R. Krausz, Electronic structure of the copper(II) ion doped in cubic KZnF3, The Journal of Chemical Physics 101 (3) (1994) 1930–1938, https://doi.org/10.1063/1.467703.
[2] A.N. Romanov, E.V. Haula, D.P. Shashkin, V.N. Korchak, Broadband Near-IR photoluminescence of trigonal-bipyramidal coordinated Cu2+ impurity center in YGaO3, YInO3 and GdInO3 hexagonal phases, J. Lumin. 228 (2020) 117652, https://doi.org/10.1016/j.jlumin.2020.117652.
[3] Y.-J. Li, S. Ye, C.-H. Wang, X.-M. Wang, Q.-Y. Zhang, Temperature-dependent near-infrared emission of highly concentrated Cu2+ in CaCuSi4O10 phosphor, J. Mater. Chem. C 2 (48) (2014) 10395–10402, https://doi.org/10.1039/C4TC01966K.
[4] Y. Zorenko, T. Voznyak, R. Turchak, Luminescence of $Cu^{+}$ and $Cu^{2+}$ Ions in CsBr Crystals, Acta Physica Polonica A 117(1) (2010) 199-202. 10.12693/APhysPolA.117.199.
[5] L. Wang, C. Wang, Y. Chen, Y. Jiang, L. Chen, J. Xu, B. Qu, H.T. Hintzen, Red-emitting SrGa2O4:Cu2+ phosphor with super-long persistent luminescence, Chem. Mater. 34 (22) (2022) 10068–10076, https://doi.org/10.1021/acs.chemmater.2c02748.
[6] D.J. Lee, Y.S. Lee, H.J. Noh, Multicolor tunable emission induced by Cu ion doping of perovskite zirconate, J. Lumin. 169 (2016) 128–131, https://doi.org/10.1016/j.jlumin.2015.08.067.
[7] Y. Zhao, D. Peng, G. Bai, Y. Huang, S. Xu, J. Hao, Multiresponsive emissions in luminescent ions doped quaternary piezophotonic materials for mechanical-to-

optical energy conversion and sensing applications, Adv. Funct. Mater. 31 (22) (2021) 2010265, https://doi.org/10.1002/adfm.202010265.
[8] Y. Zhao, G. Bai, Y. Huang, Y. Liu, D. Peng, L. Chen, S. Xu, Stimuli responsive lanthanide ions doped layered piezophotonic microcrystals for optical multifunctional sensing applications, Nano Energy 87 (2021) 106177, https://doi.org/10.1016/j.nanoen.2021.106177.
[9] A. Guo, Q. Zhu, S. Zhang, X. Sun, J.-G. Li, A building-block strategy for dynamic anti-counterfeiting by using (Ba, Sr)Ga2O4:Sm3+ new red persistent luminescent phosphor as an important component, Ceram. Int. 49 (3) (2023) 4622–4630, https://doi.org/10.1016/j.ceramint.2022.09.349.
[10] H. Klym, I. Karbovnyk, A. Luchechko, Y. Kostiv, A.I. Popov, Extended Positron-Trapping Defects in the $Eu^{3+}$-Doped $BaGa_2O_4$ Ceramics Studied by Positron Annihilation Lifetime Method, physica status solidi (b) 259(8) (2022) 2100485. 10.1002/pssb.202100485.
[11] X. Ma, P. Feng, Y. Wang, S. Ding, S. Tian, Y. Wang, Design of efficient color-tunable long persistent luminescence phosphor BaGa2O4:Pr3+ and its performance enhancement via a trap-induced strategy, J. Mater. Chem. C 10 (3) (2022) 1105–1117, https://doi.org/10.1039/D1TC04763A.
[12] M.S. Anju, N. Gopakumar, P.S. Anjana, M.R. Revupriya, Luminescence characteristics of white light emitting BaGa2O4:Dy3+ phosphors for LEDs and stress sensing applications, Radiat. Phys. Chem. 212 (2023) 111065, https://doi.org/10.1016/j.radphyschem.2023.111065.
[13] Q. Yang, R. Abdurahman, T. Yang, X. Sun, Wavelength-tunable barium gallate persistent luminescence phosphors with enhanced luminescence, Chinese Optics Letters 20 (3) (2022) 031602, https://doi.org/10.3788/col202220.031602.
[14] H. Sun, Q. Zhu, J.-G. Li, Local charge regulation by doping Li+ in BaGa2O4:Bi3+ to generate multimode luminescence for advanced optical Morse code, Ceram. Int. 48 (7) (2022) 9640–9650, https://doi.org/10.1016/j.ceramint.2021.12.163.
[15] R.E. Rojas-Hernandez, F. Rubio-Marcos, M.Á. Rodriguez, J.F. Fernandez, Long lasting phosphors: $SrAl_2O_4$:Eu, Dy as the most studied material, Renewable and Sustainable Energy Reviews 81 (2018) 2759–2770, https://doi.org/10.1016/j.rser.2017.06.081.
[16] B. Qu, B. Zhang, L. Wang, R. Zhou, X.C. Zeng, Mechanistic study of the persistent luminescence of CaAl2O4:Eu, Nd, Chem. Mater. 27 (6) (2015) 2195–2202, https://doi.org/10.1021/acs.chemmater.5b00288.
[17] Y. Lin, Z. Tang, Z. Zhang, Preparation of long-afterglow $Sr_4Al_{14}O_{25}$-based luminescent material and its optical properties, Mater. Lett. 51 (1) (2001) 14–18, https://doi.org/10.1016/s0167-577x(01)00257-9.
[18] X. Zhang, J. Zhang, Z. Nie, M. Wang, X. Ren, X.-J. Wang, Enhanced red phosphorescence in nanosized CaTiO3:Pr3+ phosphors, Appl. Phys. Lett. 90 (15) (2007), https://doi.org/10.1063/1.2722205.
[19] X. Yu, X. Xu, S. Xin, J. Qiu, Observation of energy transfer from host to rare-earth ions in Ca2SnO4:Pr3+ phosphor, J. Am. Ceram. Soc. 94 (4) (2011) 985–987, https://doi.org/10.1111/j.1551-2916.2011.04415.x.
[20] A. Wiatrowska, E. Zych, Traps formation and characterization in long-term energy storing $Lu_2O_3$:Pr Hf Luminescent Ceramics, The Journal of Physical Chemistry C 117 (22) (2013) 11449–11458, https://doi.org/10.1021/jp312123e.
[21] X. Xu, Y. Wang, W. Zeng, Y. Gong, Luminescence and storage properties of sm-doped alkaline-earth atannates, J. Electrochem. Soc. 158 (10) (2011) J305, https://doi.org/10.1149/1.3617886.
[22] J. Wang, H. Zhang, B. Lei, H. Dong, H. Zhang, Y. Liu, M. Zheng, Y. Xiao, Optical energy storage properties of (Ca1−xSrx)2Si5N8: Eu2+, Tm3+ solid solutions, J. Am. Ceram. Soc. 98 (6) (2015) 1823–1828, https://doi.org/10.1111/jace.13521.
[23] D. Dutczak, C. Ronda, A. Meijerink, T. Jüstel, Red luminescence and persistent luminescence of Sr3Al2O5Cl2:Eu2+, Dy3+, J. Lumin. 141 (2013) 150–154, https://doi.org/10.1016/j.jlumin.2013.02.012.
[24] A. Kohan, G. Ceder, D. Morgan, C. Van de Walle, First-principles study of native point defects in ZnO, Physical Review B 61 (22) (2000) 15019–15027, https://doi.org/10.1103/PhysRevB.61.15019.
[25] V. Kahlenberg, R.X. Fischer, J.B. Parise, The stuffed framework structure of $BaGa_2O_4$, J. Solid State Chem. 154 (2) (2000) 612–618, https://doi.org/10.1006/jssc.2000.8903.
[26] R.D. Shannon, Revised effective ionic radii and systematic studies of interatomic distances in halides and chalcogenides, Acta Crystallographica Section a: Found Crystallogr 32 (5) (1976) 751–767, https://doi.org/10.1107/S0567739476001551.
[27] R.P. Vasquez, $Cu_2O$ by XPS, Surf. Sci. Spectra 5 (4) (1998) 257–261, https://doi.org/10.1116/1.1247881.
[28] R.P. Vasquez, CuO by XPS, Surf. Sci. Spectra 5 (4) (1998) 262–266, https://doi.org/10.1116/1.1247882.
[29] X. Xu, Q. Shao, L. Yao, Y. Dong, J. Jiang, Highly efficient and thermally stable Cr3+-activated silicate phosphors for broadband near-infrared LED applications, Chem. Eng. J. 383 (2020) 123108, https://doi.org/10.1016/j.cej.2019.123108.
[30] H. Li, J. Cai, R. Pang, G. Liu, S. Zhang, L. Jiang, D. Li, C. Li, J. Feng, H. Zhang, A strategy for developing thermal-quenching-resistant emission and super-long persistent luminescence in $BaGa_2O_4:Bi^{3}$+, J. Mater. Chem. C 7 (42) (2019) 13088–13096, https://doi.org/10.1039/C9TC04963K.
[31] J.L. Pascual, B. Savoini, R. González, Electronic absorption spectra of Cu2+ in MgO: Ab initio theory and experiment, Physical Review B 70 (4) (2004) 045109, https://doi.org/10.1103/PhysRevB.70.045109.
[32] S.-I. Hirako, R. Onaka, Charge transfer bands of LiX: Cu2+ (X: Cl, Br) and their MCD spectra, J. Phys. Soc. Jpn. 50 (5) (1981) 1637–1644, https://doi.org/10.1143/JPSJ.50.1637.
[33] Y. Zhuang, S. Tanabe, Forward and back energy transfer between Cu2+ and Yb3+ in Ca1−xCuSi4O10: Ybx crystals, J. Appl. Phys. 112 (9) (2012) 093521, https://doi.org/10.1063/1.4765013.
[34] J. Ghijsen, L.H. Tjeng, J. van Elp, H. Eskes, J. Westerink, G.A. Sawatzky, M. T. Czyzyk, Electronic structure of $Cu_2O$ and CuO, Physical Review B 38 (16) (1988) 11322–11330, https://doi.org/10.1103/PhysRevB.38.11322.
[35] A.K. Mishra, A. Roldan, N.H. de Leeuw, CuO surfaces and CO2 activation: a dispersion-corrected DFT+U study, The Journal of Physical Chemistry C 120 (4) (2016) 2198–2214, https://doi.org/10.1021/acs.jpcc.5b10431.
[36] Y. Maimaiti, M. Nolan, S.D. Elliott, Reduction mechanisms of the CuO(111) surface through surface oxygen vacancy formation and hydrogen adsorption, Phys. Chem. Chem. Phys. 16 (7) (2014) 3036–3046, https://doi.org/10.1039/C3CP53991A.
[37] X. Chen, Z. Xia, Luminescence properties of Li2Ca2ScV3O12 and Li2Ca2ScV3O12: Eu3+ synthesized by solid-state reaction method, Opt. Mater. 35 (12) (2013) 2736–2739, https://doi.org/10.1016/j.optmat.2013.06.008.
[38] A.J.J. Bos, Theory of thermoluminescence, Radiation Measurements 41 (2006) S45–S56, https://doi.org/10.1016/j.radmeas.2007.01.003.
[39] J.T. Randall, M.H.F. Wilkins, M.L.E. Oliphant, Phosphorescence and electron traps - I. The study of trap distributions, Proceedings of the Royal Society of London. Series A. Mathematical and Physical Sciences 184(999) (1945) 365-389. 10.1098/rspa.1945.0024.
[40] A. Bessière, A. Lecointre, K.R. Priolkar, D. Gourier, Role of crystal defects in red long-lasting phosphorescence of CaMgSi2O6: Mn diopsides, J. Mater. Chem. 22 (36) (2012) 19039–19046, https://doi.org/10.1039/C2JM32953K.